

ALMA MATER STUDIORUM · UNIVERSITÀ DI BOLOGNA

---

Scuola di Scienze  
Dipartimento di Fisica e Astronomia  
Corso di Laurea in Fisica

# Study of background in the CMS barrel muon detectors with LHC Run2 data

Relatore:

Dott. Luigi Guiducci

Presentata da:

Martina Foschi

Correlatore:

Dott.ssa Francesca R. Cavallo

Anno Accademico 2017/2018



## **Abstract**

The Large Hadron Collider is the particle accelerator built at Cern where every year dozens of PetaBytes of data from proton-proton and heavy ions collisions are collected. The Compact Muon Solenoid (CMS) is one of the main detectors at LHC. CMS is a general purpose detector designed to search for signatures of new physics, and since many of these signatures include muons, it is constructed with subdetectors to identify them. In this thesis we will focus on the Drift Tube subdetector (DT) which covers the barrel part, in particular on background studies. Actually, high levels of background can cause an early ageing of the detector and could affect the muon trigger performance and pattern recognition of muon tracks. Because of that, our main goal was to assess the origin of background which mainly affects the innermost and outermost stations.



# Contents

<b>Introduction</b> .....	<b>5</b>
<b>1 LHC and Particle Physics</b>	<b>7</b>
1.1 The LHC at CERN . . . . .	7
1.2 Physics at the Large Hadron Collider . . . . .	10
1.2.1 Beyond the Standard Model . . . . .	12
<b>2 The Compact Muon Solenoid experiment</b>	<b>14</b>
2.1 The CMS detector . . . . .	15
2.1.1 The Drift Tube chambers system . . . . .	17
2.2 Muon Triggering and Reconstruction . . . . .	21
2.2.1 The Trigger system . . . . .	21
2.2.2 Muon reconstruction . . . . .	22
<b>3 Background studies</b>	<b>24</b>
3.1 Measurement techniques . . . . .	24
3.2 Background in the DT chambers . . . . .	25
<b>4 Study of DT reconstructed background segments</b>	<b>27</b>
4.1 Main tools used for the analysis . . . . .	27
4.1.1 Dataset used . . . . .	28
4.2 Analysis workflow . . . . .	28
4.2.1 One-dimensional study . . . . .	28
4.2.2 Two-dimensional study . . . . .	30
4.2.3 Results . . . . .	31
4.2.4 Background in MB4 stations . . . . .	37
<b>Conclusions</b> .....	<b>41</b>
<b>Bibliography</b> .....	<b>42</b>



# Introduction

The Large Hadron Collider is the particle accelerator built at Cern where every year dozens of PetaBytes of data from proton-proton and heavy ions collisions are collected. LHC consists of a 27 km ring where four main detectors are placed. The Compact Muon Solenoid is one of them. CMS is a general purpose detector designed to search for signatures of new physics, and since many of these signatures include muons, it is constructed with subdetectors to identify them. These latter are the Cathode Strip Chambers (CSC), the Resistive Plate chambers (RPC) and the Drift Tube chambers (DT), which surround the interaction point. In this thesis we will focus on the DT chambers, especially on background studies. Background analysis is crucial for the detector: background could affect the muon trigger performance and pattern recognition of muon tracks, and, most important, it could cause detector ageing. Because of that, our main goal was to assess the origin of background which mainly affects the innermost and outermost stations. Our approach was to classify the track segments reconstructed within individual DT chamber either as signal or background based on the information of reconstructed muon tracks. We used position and direction information associated to the segments to investigate their origin within the CMS detector volume.

The first chapter of this work introduces the LHC accelerator and provides a brief explanation of the main physics goals of the experiments studying LHC collisions.

In chapter 2 we discuss the Compact Muon Solenoid detector components, with greater details about the drift tube chambers in the first section, and the muon trigger and reconstruction in the second section.

In chapter 3 we present background measurement techniques and introduce the background characteristics in the drift tube chambers.

Finally, in the last chapter we present the analysis performed in this thesis and discuss the results we obtained.





# Chapter 1

## LHC and Particle Physics

### 1.1 The LHC at CERN

The Large Hadron Collider (LHC) is the particle collider built at CERN, in the location that previously hosted the Large Electron Positron collider (LEP). Its main goal, is both providing extremely accurate experimental evidences for the Standard Model and discovering new physics inside the SM or even beyond it, thanks to its ever growing technology.

LHC consists of a 27 km ring of superconducting material and accelerating structures whose goal is to both boost and manipulate the trajectory of running particles, namely protons and heavy ions.

These particles are particularly fit for the LHC experiments as protons and heavy ions suffer from a reduced energy loss due to synchrotron radiation. Heavy ions, moreover, allow to recreate early universe conditions possibly providing informations about the primeval Quark-Gluon plasma.

Particles travel inside pipes kept at ultra high vacuum conditions in two separate beams, one running clockwise and one running counter-clockwise. Here magnetic n-poles, working at 1.9 K thanks to a Helium-fuelled cryogenic system, are used to curve and focus the beam's trajectory. For instance, magnetic dipoles provide beam bending while other n-poles are employed to improve the focus of the beam, the goal being to maximize the Luminosity. This latter is defined as the quantity that measures the ability of a particle accelerator to produce the required number of interactions; quantitatively, the Luminosity ( $\mathcal{L}$ ) is the proportionality factor between the ratio of events per second and the production cross-section following from :

$$\frac{dR}{dt} = \mathcal{L} \cdot \sigma_p \quad (1.1)$$

LHC luminosity design value is about  $10^{34} \text{ cm}^{-2}\text{s}^{-1}$ . After operating at this value for some years a new project, High Luminosity LHC (HL-LHC), has begun.

The HL-LHC project aims to rise the performance of the accelerator in order to increase the potential for discoveries after 2025. The objective is to increase luminosity by a factor of 10 beyond the LHC's actual design value.

Particle injection in LHC is done employing pre-existing accelerators, following those steps:

- Protons are injected inside the Linear Accelerator LINAC2, that makes them reach 50 MeV;
- then particles pass through the Booster reaching 1.4 GeV;
- in the Proton Synchrotron (PS) protons are accelerated up to 0.99c, thus reaching 25 GeV;
- the Super Proton Synchrotron (SPS), which is a sub-ring of 7 Km, makes the particles reach 450 GeV;
- the beam is finally injected into the LHC ring, where it gets accelerated up to the final center-of-mass energy of 13 TeV.

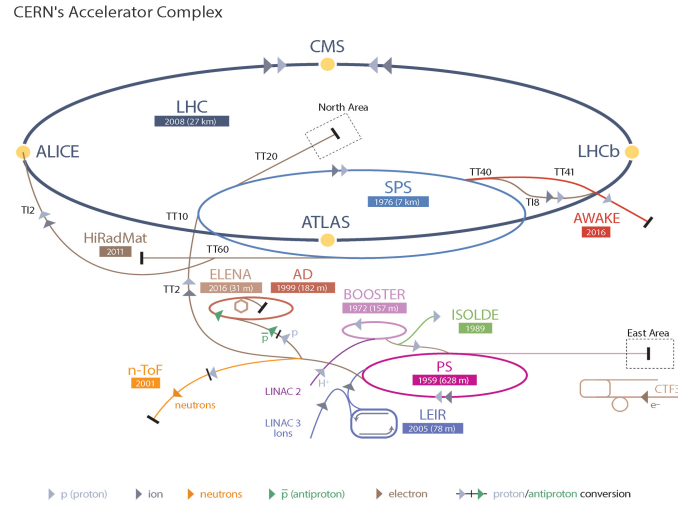


Figure 1.1: LHC Complex

The LHC beam filling requires about two hours. The beam lifetime is about 22 hours, however data are usually taken only in the first 10 hours, then the beams are dumped and a new fill is started in order to restart at maximum beam intensity to maximize the integrated luminosity collected by the detectors. Beams have a bunched structure with a crossing frequency  $f = 40\text{MHz}$ , corresponding to a time between collisions of  $25\text{ns}$ .

Bunches contains about  $N = 1.1 \cdot 10^{11}$  protons each.

There are seven experiment currently installed at LHC, four of which are considered the main ones:

- ALICE is a detector whose goal is to study heavy ion colisions giving special attention to Quark-Gluon plasma phenomena and the restoration of the chiral symmetry.

size	26m(length), 16m(height), 16m(width)
weight	10000 tons
location	Sergy (France)

- ATLAS is a multipurpose detector able to cover a wide variety of phenomena from high precision measurements to the discovery of new physics.

size	46m(length), 26m(height), 26m(width)
weight	7000 tons
location	Meyrin(Switzerland)

- CMS detector is another multi-purpose detector with a very different technical design with respect to ATLAS. Further informations will be given in Chapter 2.

size	21m(length), 15m(height), 15m(width)
weight	12500 tons
location	Cessy (France)

- LHCb is specialized in studying the asymmetry between matter and anti-mater in processes involving particles containing  $b$  quark.

size	21m(length), 10m(height), 13m(width)
weight	5600 tons
location	Ferney-Voltaire (France)

## 1.2 Physics at the Large Hadron Collider

The Standard Model (SM) is currently the most advanced theory we can use to describe the complex nature of subnuclear phenomena. Starting from a small cluster of particles and three fundamental forces, mathematically expressed via Gauge theory, the SM provides an accurate description of particle physics.

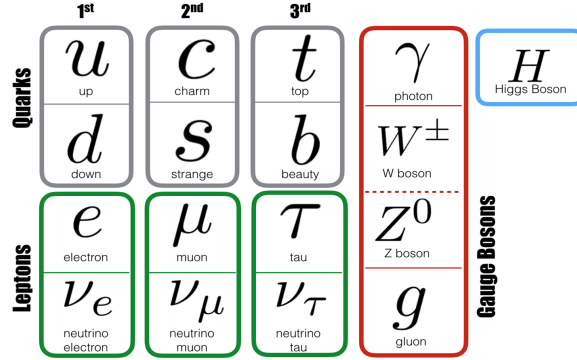


Figure 1.2: Standard Model

The particles in the SM can be split in two macro-groups: Fermions and Bosons. Fermions obey to Fermi-Dirac Statistics and, most importantly, Pauli's exclusion principle. Bosons, on the other hand, obey to the Bose-Einstein Statistics. This difference will have, for instance, crucial consequences in the mathematical treatment of nuclei. Focusing on Fermions, we can split them into two further families: Leptons and Quarks. Leptons ( $e, \mu, \tau$ ) have unitary charge, defined in terms of single electron charge ( $e = 1.6 \cdot 10^{-13} \text{C}$ ) and they interact only via the Electromagnetic force. There are three other leptons, namely the three types of Neutrino ( $\nu_e; \nu_\mu; \nu_\tau$ ) whose charge is strictly zero and the interaction they undergo is only the Weak one. Each Lepton has its own AntiLepton, this latter being a particle with same mass as the former but endowed with opposite electric charge.

Particle	Mass(MeV)	Charge( $e$ )
$e$	0.5	-1
$\mu$	106	-1
$\tau$	1770	-1
$\nu_e$	$< 2 \cdot 10^{-6}$	0
$\nu_\mu$	$< 0.19 \cdot 10^{-6}$	0
$\nu_\tau$	$< 18.2 \cdot 10^{-6}$	0

Table 1.1: Masses and charges of Leptons.

Quarks ( $u, c, t, d, s, b$ ) are subject to all the SM interactions and have half integer charge (see table 1.2). We can classify these particles introducing a new quantum number called flavour; for more details see Table 1.3.

Each Quark has its own AntiQuark, a particle with same mass but opposite electric charge.

Quarks have not been directly observed since a well comprehended property of their nature, namely “Confinement”, makes apparently impossible to disengage and isolate a single Quark.

Thus, only bound states of Quarks, expressely Hadrons, have been observed.

We can split the whole Hadron family in two branches: Mesons and Baryons, their difference being in the internal composition.

Mesons are in fact composed by a Quark-AntiQuark couple whereas Baryons are formed by a triplet of Quarks or AntiQuarks.

particle	Mass(MeV)	Charge( $e$ )
$u$	350	$\frac{2}{3}$
$c$	1500	$\frac{2}{3}$
$t$	180000	$\frac{2}{3}$
$d$	350	$-\frac{1}{3}$
$s$	500	$-\frac{1}{3}$
$b$	4500	$-\frac{1}{3}$

**Table 1.2:** Masses and charges of Quarks.

particle	Isospin( $I, I_3$ )	Charm(C)	Beauty(B)	Strangeness(S)	Topness(T)
$u$	$(1, \frac{1}{2})$	0	0	0	0
$c$	0	1	0	0	0
$t$	0	0	0	0	1
$d$	$(1, \frac{1}{2})$	0	0	0	0
$s$	0	0	0	-1	0
$b$	0	0	-1	0	0

**Table 1.3:** Classification of Quarks via Flavour quantum numbers.

We shall now take a closer look to interactions.

In Nature, four interactions are known to exist: Gravitational, Strong, Weak and Electromagnetic. The SM, by the way, is able to provide a quantitative description only as far as the last three are taken into account. The mathematical frame used to do so is the Gauge theory.

Basically the main idea behind Gauge theory is the following: taking into account a given system, its Lagrangian is written down and its symmetries, which are valid in each

point of the space (global symmetry), get tracked down. Then, an Ansatz is made: the Lagrangian should have also local symmetries which can be deduced from the global ones.

Thus we introduce a gauge field whose property is to correctly couple particles to fields. The symmetry underlying the SM, expressed in group formalism, is the following:

$$SU(3) \times [SU(2) \times U(1)]$$

The dimension of each representation is connected to the number of charges involved in the interaction.

$SU(3)$  represents the Strong interaction and predicts three charges, which happen to be the colour charges (red, blue, green) of Quarks, and eight fields, that correspond to Gluons<sup>1</sup>.

$SU(2)$  is connected to the Weak interaction and correctly predicts two charges involved, the Isospin couple, and three fields ( $Z^0$ ;  $W^\pm$  bosons).

$U(1)$  represents the Electromagnetic interaction and only one charge is theoretically needed.

### 1.2.1 Beyond the Standard Model

The Standard Model of particle physics agrees very well with experiments, but many physical phenomena in nature are not adequately explained. For example the SM does not explain gravity. The approach of simply adding a “*graviton*” to the theory does not account what is observed experimentally. On the other hand, the SM cannot be included in the most successful Einstein’s theory of general relativity.

Another problem which the SM does not answer to is the presence of dark matter. Cosmological observations tell us the standard model explains about 5% of the energy present in the universe. About 26% should be dark matter which only interacts weakly with the Standard Model fields. Yet, the SM does not supply any fundamental particles that are consistent dark matter candidates.

The remaining 69% of the energy in the universe should be so called “dark energy”, a constant energy density for the vacuum. Attempts to explain dark energy in terms of vacuum energy of the SM lead to a mismatch of 120 orders of magnitude.

As we can see from figure 1.3, neutrinos are massless particles in the context of the Standard Model. However neutrinos oscillation experiments have shown that neutrinos do have mass. Mass terms can be added to the theory “by hand”, but this lead to new theoretical problems. For instance, the mass terms need to be extrimely small and it is not clear if the neutrino masses would arise in the same way as the masses of other

---

<sup>1</sup>This is obtained following Yang-Mills theory. Given a representation dimension  $N$ , the number of gauge fields involved is exactly  $N^2 - 1$

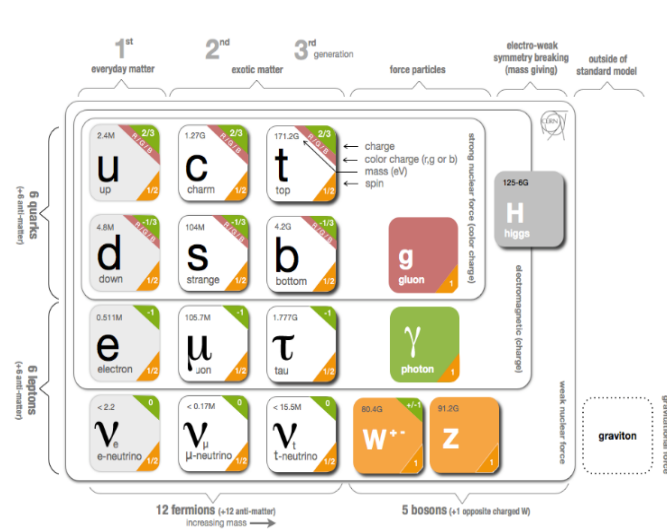


Figure 1.3: Physics beyond the Standard Model

fundamental particles do in the Standard Model.

Finally there is the crucial problem of matter-antimatter asymmetry. The Universe is made out of mostly matter. However, the standard model predicts that matter and antimatter should have been created in equal ammounts if the initial conditions of the universe did not involve disproportionate matter relative to antimatter. Yet, no mechanism to explain this asymmetry exists in the Standard Model. It is because of these unsolved problems that experimental physicists continue to upgrade and improve experiments to investigate nature.

## Chapter 2

# The Compact Muon Solenoid experiment

The Compact Muon Solenoid (CMS) detector at CERN LHC is a general purpose device designed to search for signatures of new physics in proton-proton and heavy ion collisions. Since many of these signatures include muons, CMS is constructed with subdetectors to identify muons, trigger the CMS readout upon their detection, and measure their momentum and charge over a broad range of kinematic parameters.

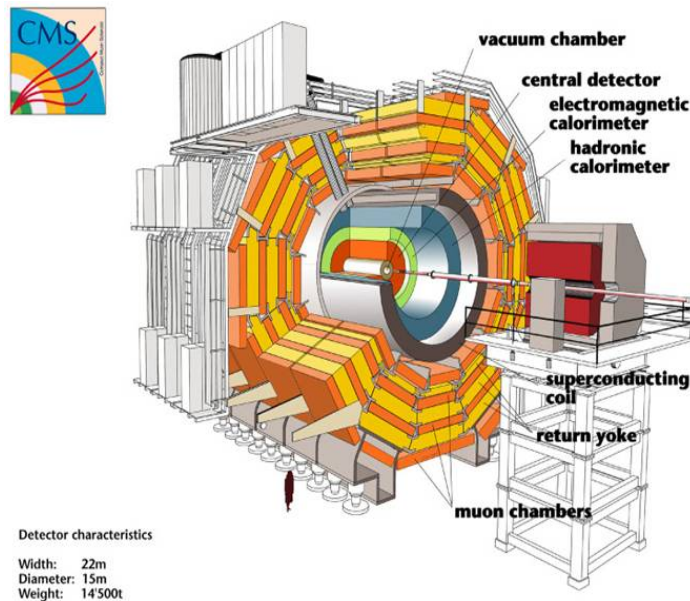


Figure 2.1: The Compact Muon Solenoid

Kinematics in CMS is described according to a right-handed coordinate system where the origin is placed in the p-p interaction point. The z axis is along the beam pipe, the



abscissa points at the centre of LHC and the ordinates points upwards. Polar coordinates  $(R, \theta, \phi)$  are often used to describe kinematics of collision products. The polar angle  $\theta$  is defined in the  $zy$  plane, while the azimuthal angle  $\phi$  is defined in the  $xy$  plane. In this latter the track bending in the magnetic field happens and the momentum component on this plane is called transverse momentum  $p_T$ . Another significant parameter, often used in collider physics, is the rapidity defined as

$$y = -\frac{1}{2} \ln \frac{E + p_z}{E - p_z} \quad (2.1)$$

since it is invariant for Lorentz boost. Considering that rapidity depends on quantities that can't be directly measured, a further crucial parameter is the pseudorapidity defined as

$$\eta = -\frac{1}{2} \ln \frac{\theta}{2} \quad (2.2)$$

Pseudorapidity approximates rapidity in the ultra relativistic regime.

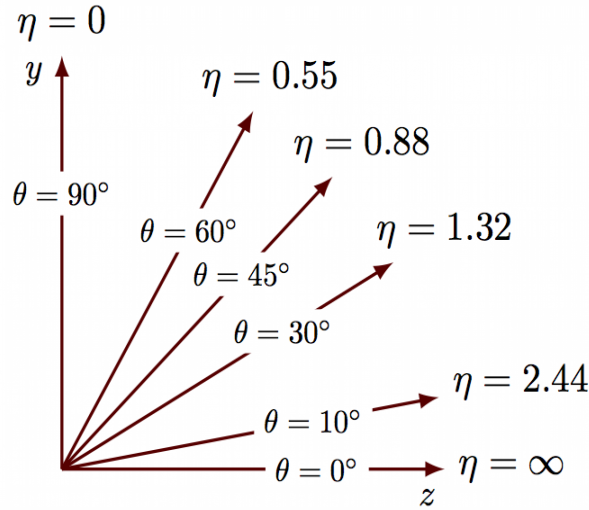


Figure 2.2: Pseudorapidity range

## 2.1 The CMS detector

The CMS detector has a cylindrical geometry with several concentric layers of components [1]. The innermost element of the detector is the Silicon Tracker which records paths taken by charged particles, bended by the 3.8T magnetic field produced by the solenoid magnet, finding their positions at a number of key points. The tracker can

reconstruct paths of high-energy muons, electrons and hadrons as well as see tracks coming from the decay of very short-lived particles. In view of this variety of particles the detector includes two kinds of calorimeters. The Electromagnetic Calorimeter (ECAL), the internal layer of the two, measures the energy of electrons and photons by stopping them completely. Conversely hadrons, made up by quarks and gluons, fly through the ECAL and are stopped by the outer layer called the Hadron Calorimeter (HCAL).

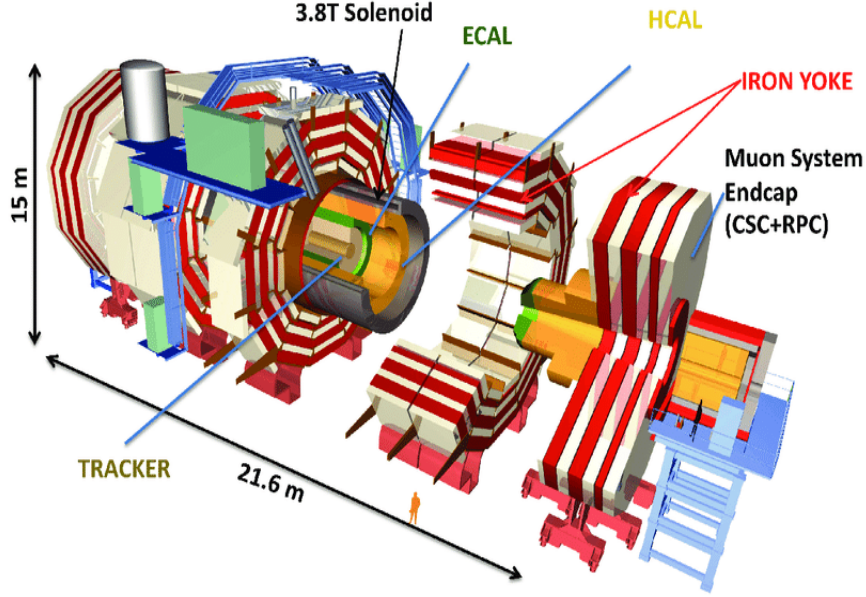


Figure 2.3: CMS components

As previously mentioned, CMS main goal is to detect muons, which can penetrate several metres of iron without interacting, unlike most of particles that are stopped by calorimeters. Therefore, the muon system is located outside the solenoid and it is composed of gaseous detectors, interposed among the layers of the steel flux-return yoke, that allow a traversing muon to be detected at multiple points along the track path. Muon system is composed of three types of gas ionization chambers, DT, CSC and RPC. The drift tubes chambers (DT) are segmented into drift cells so the position of muons is determined by measuring the drift time to an anode wire of a cell with a shaped electric field. The cathode strip chambers (CSC) operate as standard multi-wire proportional counters but add a finely segmented cathode strip readout, which yields an accurate measurement of the position of the bending plane ( $R-\phi$ ) coordinate at which the muon crosses the gas volume. The resistive plate chambers (RPC) are double-gap chambers operated in avalanche mode and are primarily designed to provide timing information for the muon trigger. The DT and CSC chambers are located in the regions  $|\eta| < 1.2$  and  $0.9 < |\eta| < 2.4$  respectively, and are complemented by RPCs in the range

$|\eta| < 1.9$ . Three regions can be distinguished, naturally defined by cylindrical geometry of the detector, referred to as the barrel  $|\eta| < 0.9$ , overlap  $0.9 < |\eta| < 1.2$  and endcap  $1.2 < |\eta| < 2.4$  regions. In the barrel a station is a ring of chambers assembled between two layers of the steel flux-return yoke at approximately the same value of radius  $R$ . There are four DT and four RPC stations in the barrel, labeled MB1-MB4 and RB1-RB4, respectively. Conversely in the endcaps a station is a ring of chambers assembled between two disks of steel flux-return yoke at approximately the same value of  $z$ . There are four CSC and four RPC stations in each endcap, labelled ME1-ME4 and RE1-RE4, respectively. Between Run1 and Run2 additional chambers were added in ME4 and RE4 to increase redundancy, improve efficiency and reduce misidentification rates.

### 2.1.1 The Drift Tube chambers system

In the barrel region the muon rate is low, the neutron background is relatively small except in the outermost station MB4 and the magnetic field is mostly uniform with strength below 0.4T in between the yoke segments. Here drift chambers with standard rectangular cells and electrical field shaping are employed. The DT detector is composed by 5 wheels along the beam direction ( $z$ ). They are called “YB ”(Yoke Barrel) and are organized into 12  $\phi$ -segments per wheel, forming four stations at different radii interspersed between plates of the magnetic flux return yoke called MB1-MB4. Each station consists of eight layers of tubes measuring the position in the bending plane and four layers in the longitudinal plane.

The basic element of the DT system is the drift cell which has a transverse size of  $42 \times 13\text{mm}^2$  with a  $50\mu\text{m}$  diameter gold-plated stainless steel anode wire at the center that operates at +3600 V. The gas mixture(85%/15% of Ar/CO<sub>2</sub>) provides good quenching properties and a saturated drift velocity of about  $55\mu\text{m/ns}$ . The maximum drift time is almost 400ns. The cell design uses four electrodes to shape the effective drift field, two on the side walls of the tube and two above and below the wires on the ground planes between the layers. Four staggered layers form a superlayer (SL), while a chamber consists of two superlayers that measure the  $r - \phi$  coordinates with wires parallel to the beam line, and a orthogonal superlayer that measures the  $r - z$  coordinate. This is except from the MB4 which has only an  $r - \phi$  superlayer.

Chambers are limited in size in the longitudinal direction by the segmentation of the barrel yoke and are about 2.5 m long. On the transverse size their length varies with the station ranging from 1.9 m, for MB1, to 4.1 m for MB4.

The DT and CSC muon detector elements together cover the full CMS pseudorapidity interval  $|\eta| < 2.4$  with no acceptance gap, ensuring good muon identification over a range corresponding to  $10^\circ < \theta < 170^\circ$ . Offline reconstruction efficiency for the muons is typically 96 – 99% except in the gaps between the five wheels of the yoke and the

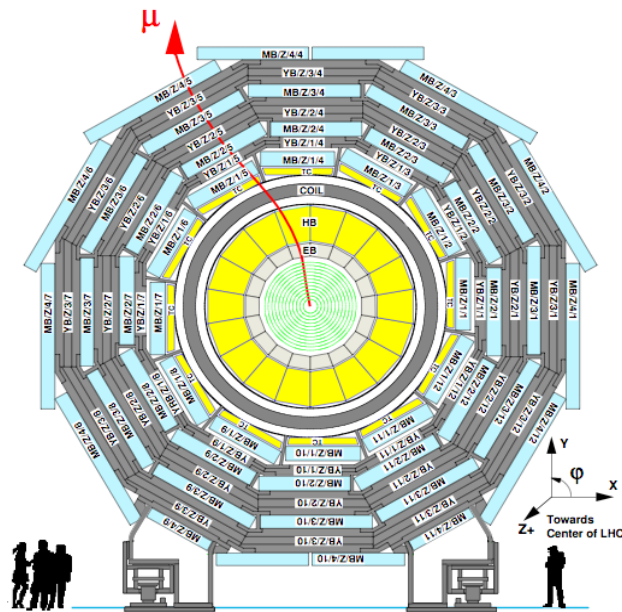


Figure 2.4: CMS azimuthal view

transition region between the barrel outer wheels and the endcap disks. The amount of absorbing material before the first muon station reduces the contribution of punch-through particle to about 5% of all muons reaching the first station and to about 0.2% of all muons reaching further muon stations. Crucial properties of the DT system are that it can identify the collision bunch crossing that generated the muon and trigger on the  $p_T$  of muons with good efficiency and that it has the ability to reject background by means of timing discrimination.

## The DT system calibration

Charged particles, crossing a drift cell in the DTs, ionize the gas in the cell. The drift time of the ionization electrons is obtained by using a time-to-digital converter (TDC), after subtracting a time pedestal. This latter contains contributions from the latency of the trigger and from the propagation time of the signal within the detector and the data acquisition chain. The hit position is reconstructed as

$$x_{hit} = t_{drift} \cdot v_{drift} = (t_{TDC} - t_{ped}) \cdot v_{drift} \quad (2.3)$$

where  $t_{TDC}$  is the measured time,  $t_{ped}$  the time pedestal, and  $v_{drift}$  the effective drift velocity, which we assume being approximately constant in the cell volume [2].

In an ideal cell the time distribution from the TDC would have a box shape starting at close to 0 ns for muon tracks passing near the anode and extending up to 380 ns for

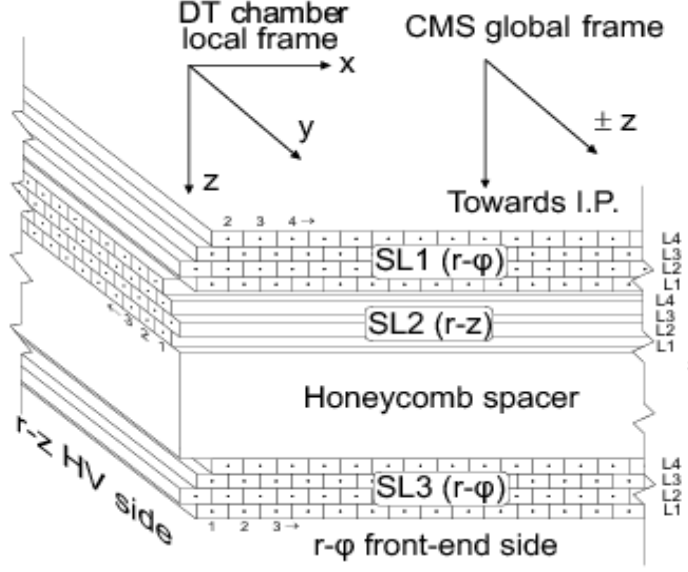


Figure 2.5: DT layers and superlayers

those passing close to the cathode. In practise different time delays related to the trigger latency and the length of the cables to the readout electronics contribute to the time measured by the TDC:

$$t_{TDC} = t_{drift} + t_0^{wire} + t_{L1} + t_{TOF} + t_{prop} \quad (2.4)$$

where the different contributions to the time pedestal are classified as

- $t_0^{wire}$ , the channel by channel signal propagation time to the readout electronics, relative to the average value in a chamber ; it is used to equalize the response of all the channel in a chamber;
- $t_{L1}$ , the latency of the Level-1 trigger;
- $t_{TOF}$ , the time of flight of the muon produced in a collision event, from the interaction point to the cell;
- $t_{prop}$ , the propagation time of the signal along the anode wire.

The inter-channel synchronisation  $t_0^{wire}$  is determined by test pulse calibration runs. It is a fixed offset since it depends only on the cable length. The remaining contribution to the time pedestal is extracted from the data for each SL. It is computed as the turn-on point of the TDC time distribution , after correction for the inter-channel synchronisation. This contribution is called  $t_{trig}$ , since is dominated by the Level-1 trigger latency and

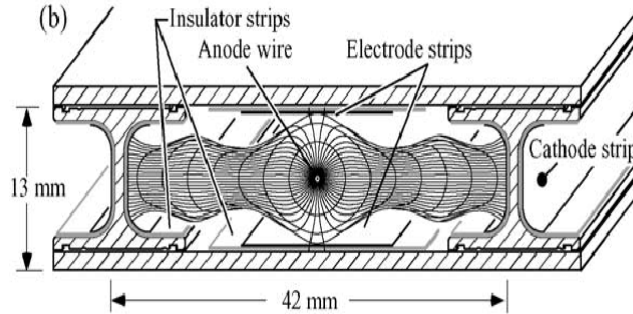


Figure 2.6: Section of a drift tube cell

includes the contributions from the average time-of-flight, as well as the average signal propagation time along the anode wire, taken from the centre of the wire to the front-end board. The correction for the propagation time along the wire and the muon time-of-flight to the cell is performed at the reconstruction level, after the 3D position of the track segment is determined. Finally to define the turn-on point of the TDC time distributions more precisely, a correction to the  $t_{trig}$  pedestal is calculated by using the hit position residuals. These latter are computed as the distance between the hit position and the intersection of the 3D segment with the layer plane.

The drift velocity depends on the gas mixture, purity and the electrostatic configuration of the cell. The effective drift velocity is further affected by the presence of the residual magnetic field and the track incidence angle and is computed as an average for each SL system. To determine the drift velocity we use two methods where the first is based on the “ mean-time ” technique and the second is based on the local muon reconstruction in which a track is fitted to measurements from one chamber at a time. The mean-time method exploits the staggering of the chamber layers. Because of the staggering, ionization electrons drift in opposite directions in even and odd layers. Therefore the maximum drift time  $t_{max}$  in a semi-cell can be calculated from the drift times of hits from the track crossing nearby cells in consecutive layers. The appropriate mean-time relation is chosen for each track by using the three-dimensional position and direction of the track segment in the SL. To determine the drift velocity we use the linear approximation

$$v_{drift}^{eff} = L_{semi-cell} / \langle t_{max} \rangle \quad (2.5)$$

where  $L_{semi-cell} = 2.3mm$  is approximately half the width of a drift cell.

An alternative method for computing the drift velocity relies on the full reconstruction of the trajectory in the muon system. A track is reconstructed by assuming the nominal drift velocity and in a second step is refitted with the drift velocity and the time of passage of the muon through the chamber as free parameters. This method is applied to the  $r - \phi$  view of the track segment in a chamber, but cannot be applied to the  $r - z$

SLs where only four points are available in the fit to disentangle the drift velocity and synchronisation contributions. Finally a notable reduction of drift velocity of about 2% is observed in the innermost chambers of the outer wheels because of the Lorentz angle induced by the stronger magnetic field.

## 2.2 Muon Triggering and Reconstruction

### 2.2.1 The Trigger system

The triggering scheme of the CMS muon system relies on two independent and complementary triggering technologies, one based on the precise tracking detectors in the barrel and endcaps, and the other based on the RPCs. The tracking detectors provide excellent position and time resolution, while the RPC system provides excellent timing but with poorer spatial resolution.

For values of the transverse momentum  $p_T$  up to 200 GeV/c, the momentum resolution is dominated by the large multiple scattering in the steel, combined in the endcaps with the effect of the complicated magnetic field that is associated with the bending of the field lines returning through the barrel yoke.

The large number of layers in each tracking chamber is exploited by a trigger hardware processor that constructs track segments in the chambers with a precision sufficient to set sharp transverse momentum thresholds at the level-1 trigger level up to 100 GeV/c, and to tag the parent bunch crossing (BX) with very good time resolution. This component of the L1 trigger is called the “local trigger” since it operates purely with information local to a chamber.

Originally the Muon Trigger was designed to preserve the complementarity and redundancy of CSC, DT and RPC which were used to build tracks separately until they were combined in the Global Muon Trigger.

Now all the hits contribute to the track whatever subsystem detects them. Furthermore the upgrade introduced a regional segmentation that treats muon tracks separately depending on  $\eta$ . It distinguishes a barrel region (low  $\eta$ ), an endcap region (high  $\eta$ ) and a transition region between them ( $|\eta| \approx 1$ ) called overlap. Such regions result in different triggering algorithms but also in different deployments of hardware processors. The final sorting and ghost track cancellation of muon candidates are handled separately for each of the three regions in  $\eta$ . Finally all the information is sent to the Global Trigger which takes the final decision whether to reject or accept the event, based on a menu of hundreds of different decision algorithms, tuned for different physics cases.

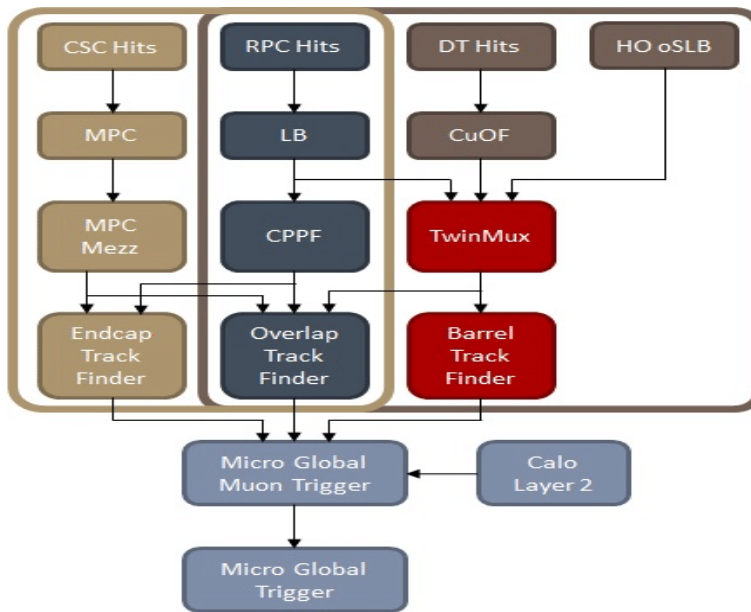


Figure 2.7: Level 1 Trigger

A suitably steep transverse momentum threshold is obtained by requiring a local spatial resolution of the segments on the order of a couple of millimetres. This resolution is necessary to guarantee a high trigger efficiency and defines a lower limit on the accuracy that must be reached by the alignment of the chamber positions.

### 2.2.2 Muon reconstruction

The geometry of CMS has a deep influence on the performance of the muon system. The change in the direction of the magnetic field in the return yoke causes the curvature of the muon trajectory to reverse. Therefore the first muon detector stations, in both the barrel and endcap regions, are critical since they provide the largest sagitta and hence the most important contribution to the measurement of the momentum of high momenta muons, for which multiple scattering effects become less significant.

Reconstruction proceeds by first identifying hits in the detection layers of a muon chamber due to the passage of a muon or another charged particle, and in the DT and CSC systems by then building straight-line track segments from these hits. Local reconstruction in DT chambers is performed in steps [3]:

- drift time is converted in a drift distance from a wire in a DT cell;
- cell hits are used to fit 2D segments independently in  $r - \phi$  (up to 8 hits) and  $r - z$  superlayers (up to 4 hits);



- the two projection are combined to build a 3D segment in the chamber which will be used in the track fit

This is referred to as local reconstruction. The reconstruction of muon tracks from these hits and segments is called global reconstruction. Muon tracks can be reconstructed by using hits in the muon detectors alone so the resulting muon candidates are called standalone muons. Alternatively the reconstruction can combine hits in the muon detectors with those in the central tracker and the resulting muon candidates are called global muons. Finally the muon system can also be used purely to tag extrapolated tracks from the central tracker which are called “tracker muons”.

At large transverse momenta,  $p_T \geq 200$  GeV, the global-muon fit improves the momentum resolution with respect to the tracker-only fit, but as the  $p_T$  value increases, the additional hits in the muon system gradually improve the overall resolution. Global muons exploits the full bending of the CMS solenoid and return yoke to achieve the ultimate performance in the TeV/c region.

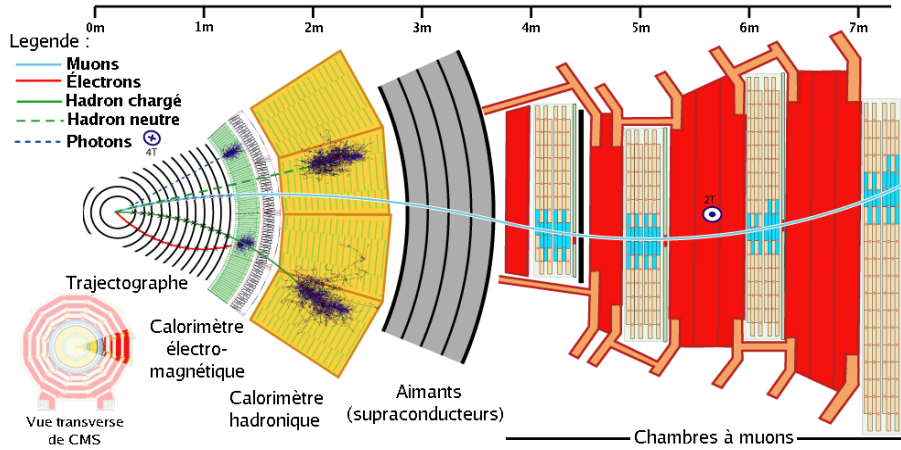


Figure 2.8: Reconstruction of a muon trajectory

Reconstructed muons are fed into the CMS particle flow (PF) algorithm. This latter combines information from all CMS subdetectors to identify and reconstruct all individual particles for each event, including electrons, neutral hadrons, and muons. For muons PF applies a set of selection criteria to candidates reconstructed with standalone, global or tracker muon algorithms.

# Chapter 3

## Background studies

Levels of background radiation in the CMS muon system can in principle affect its overall performance. Any background source, including low energy neutrons or photons, electrons and positrons, punch-through hadrons, low momentum primary and secondary muons, and in general all beam-induced background could affect the muon trigger performance and pattern recognition of muon tracks. In particular, spurious hits produced by noise or radiation background could spoil the track reconstruction and promote low transverse-momentum muons to higher momentum. Furthermore the radiation background could affect the detector performance by accelerating the CMS aging and therefore its efficiency degradation.

### 3.1 Measurement techniques

Each of the muon subsystems employ different technology and different materials, thus each one responds differently to the various backgrounds. For example, on one hand, the CSC system has six active planes per chamber and typically requires at least four out of six hits to generate a track segment. Hence, the CSCs are relatively immune to neutrons, which generally affect only a single plane. On the other hand, the CSCs cannot distinguish punch-through background particles from genuine muon tracks. The RPC system provides a single hit per chamber from two gaps, and thus it triggers on neutron hits. However, the RPC system has a very narrow time window of 25 ns and is relatively unaffected by out-of-time signals. Finally the DT system has twelve planes per chamber and the segment reconstruction is mostly immune to neutron hits as long as the rate is not too high. The time window for the DTs, however, is large that so it suffers from out-of-time background, hence high background rate could make track reconstruction difficult, and the event size could become too large for the readout. As a result of these different technologies, each subsystem measures background rates in a different manner. The CSC system measures the trigger rate per chamber. To increase

the sensitivity to background such as neutrons, the CSC trigger was to run in a special configuration that requires only a single layer coincidence of wire and strip hits within a time window of 75 ns. A coincidence of two or more hits from different layers that satisfy the single track criteria is considered in this configuration as a single triggering event. The RPC average strip rate is calculated by using the incremental counts, performed at the level of the RPC DAQ board, normalized to the strip area. The noise level is estimated of each run and each chamber separately through a linear extrapolation to a value for an instantaneous luminosity at 0, which is then subtracted from the chamber rate. After this noise subtraction, the resulting RPC rate is divided by two to account for the two RPC gaps.

Further informations about DTs will be given in the following paragraph.

## 3.2 Background in the DT chambers

The DTs consider as background detector signals that aren't produced by crossing muons. By integrating over the full  $1.25\ \mu\text{s}$  readout window, the DTs also measure rates of out-of-time background originating mainly from slow neutrons, hadron punch-through, and hits that originated from other bunch-crossings (pileup). As shown in Figure 3.1, the time distribution of these hits in the full  $1.25\ \mu\text{s}$  TDC time window is flat, in contrast to the one for signals generated by prompt muons from proton-proton collisions, which arrive roughly within a 400 ns time interval, corresponding to the drift time across an entire cell.

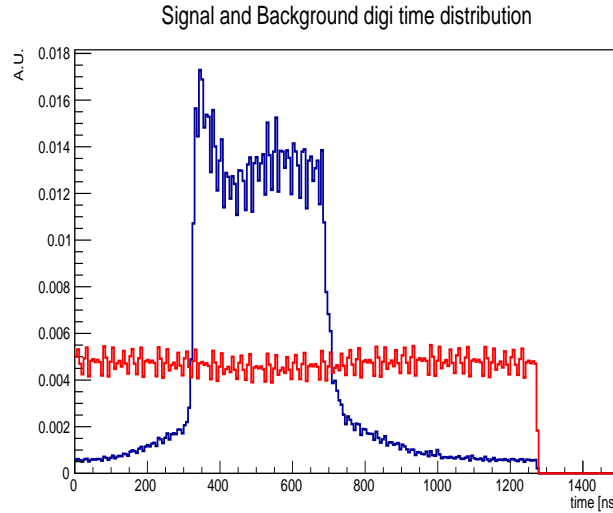


Figure 3.1: Signal (blue) and background (red) digi times

The background observed in the DT chambers has two different origins

- The so called “ neutron gas ” which is produced by colliding beams and fill the empty space between the detector and the caver’s ceiling. It is mainly responsible for the background in the external stations (MB4) of the upper sectors;
- The high particle multiplicity in the forward regions related to Pile Up: hadron punch-through and shower leaks are some of the causes of background in the internal stations (MB1), mainly in external wheels.

# Chapter 4

## Study of DT reconstructed background segments

Our main goal was to assess the origin of background which affects the DT stations. In the Run 1, study any superlayer with more than two recorded hits was discarded as being potentially crossed by a prompt muon. Furthermore in the Run1 study, only the 0 - 250 ns time range was considered for the background computation. This method is suitable to study hit background but (by definition) it can't be used to study segments. On the other hand reconstructed track segments in the muon subsystems are used to seed the muon reconstruction. Therefore monitoring background segments is crucial. For this reason we started from the approach of considering as background whatever signal is not produced by a crossing muon [6]. In order to preserve sensitivity for different types of background, the new approach consists of a tighter definition of the muon signal region and, as a consequence, a larger acceptance for background. Now we accept as background whatever hits or reconstructed segments are found within the chambers that were not crossed by reconstructed muons, and within in the full range readout by the TDC which is 1275 ns.

### 4.1 Main tools used for the analysis

The whole analysis was developed using the Root framework. Root-ples were produced starting from CMS data, in the standard format of the “ DT Tree ”, used by the DT group. This tree contains all relevant information for muon detector performance studies. For our analysis we needed information related to:

- reconstructed muons, to define the signal regions to be discarded;
- reconstructed DT segments, to check the presence of background track segments;

The muon related information that was relevant to our analysis was the list of DT chambers crossed by the muon trajectory: this was only defined for reconstructed muons that exploit the tracker information, by means of propagating the inner track to the muon stations. For what concerns standalone-muons, the list of DT segments associated in the muon reconstruction was used instead to identify the chambers to be discarded before background computation. So for every event a loop on the reconstructed muons is performed and the list of crossed chambers is registered. Having identified event by event the remaining chambers to be considered for the background evaluation, we looked at hits and segments (if any) detected within them.

### 4.1.1 Dataset used

Full event information with both raw and reconstructed data requires several MBytes of disk space per event. Therefore it is impossible to store it for all events registered by CMS, but some datasets have this informations saved for specific need of the analysis groups. Among these, the groups in charge of studying the performance of the muon detectors make use of the so called “ZMu Skim” data: sets of events triggered by a “Single muon trigger” and then selected for containing a candidate Z boson decaying into a pair of muons. The results shown in the following sections have been obtained using nearly five millions events of the ZMu Skim collected by CMS between August 28 to September 6, 2018.

## 4.2 Analysis workflow

### 4.2.1 One-dimensional study

In order to identify the origin of the background segments we first propagated them as straight lines in the  $z - R$  plane and found the intersection with the  $z$  axis (beam line). In the  $z - R$  view there is no bending of the tracks. Since we needed positions and directions for all three coordinates in the CMS global reference frame, we could only use segments that are reconstructed in both the transverse and longitudinal views. Thus, this analysis is performed only for the first three stations (MB1, MB2, MB3), as the chambers of the MB4 station have no theta Superlayer, therefore they provide no  $z$  measurements (see Section 4.2.4).

For each fully reconstructed segment, in the three inner stations, its coordinates and its director cosines are available. Such information is used to determine a straight line in the  $z - R$  plane containing the segment position and the beam line. With some basic trigonometry, we determine the  $z$  coordinate of the intersection of the straight line derived from the segment with the  $z$  axis.

Namely:

- for each segment position, we calculate its distance from the  $z$ -axis

$$r_{\perp} = \sqrt{x_S^2 + y_S^2}, \quad (4.1)$$

where  $x_S$  and  $y_S$  are the coordinates of the segment in the transverse plane, in the global reference frame;

- the angle between the segment direction and the  $z$  axis (see Figure 4.1) is defined by the relation

$$\tan \theta_S = \frac{r_{\perp}}{z_S - z_L}, \quad (4.2)$$

where  $\theta_S$  is obtained by the arc cosine of the  $z$  director cosine;

- we extract the value  $z_L$ , as

$$z_L = z_S - \frac{r_{\perp}}{\tan \theta_S} \quad (4.3)$$

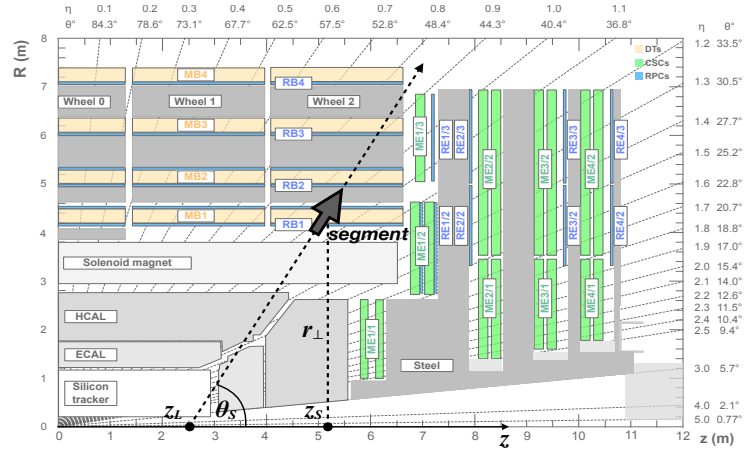


Figure 4.1: Scheme of  $z_L$  extrapolation

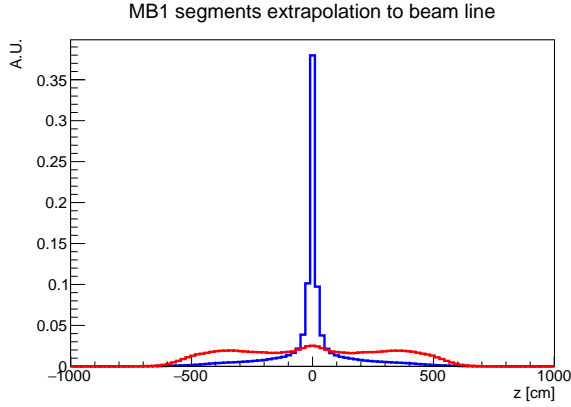


Figure 4.2: MB1 segments extrapolation to beam line

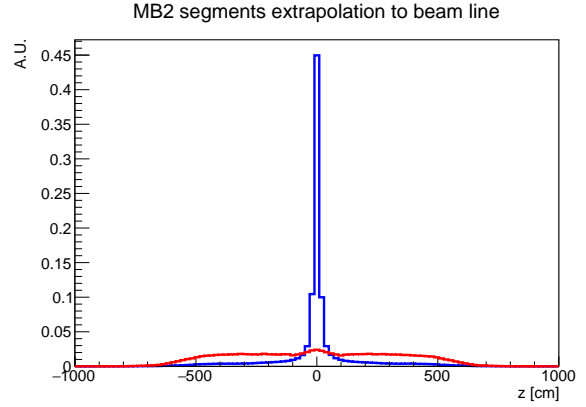


Figure 4.3: MB2 segments extrapolation to beam line

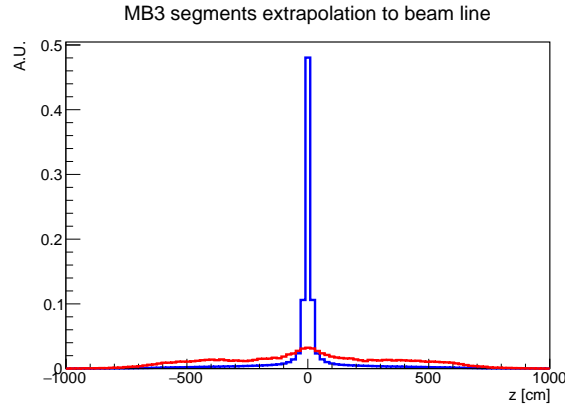


Figure 4.4: MB3 segments extrapolation to beam line

In Figures 4.2, 4.3, 4.4, the distribution of values of  $z_L$  is shown, for signal and background segments. Here we have superimposed the signal histogram (blue) to the background histogram (red) for each station, normalizing them to each other, for MB1, MB2, MB3 respectively.

## 4.2.2 Two-dimensional study

We can see that while signal segments precisely point to the region around  $z \approx 0$ , corresponding to the interaction point, background has two bumps approximately at -400 and +400 on the  $z$  axis which roughly correspond to the position of the calorimeter cracks. However we couldn't say precisely where the origin of the tracks actually was. In order to visualize it, we built a two-dimensional histogram to be filled with the straight



lines extrapolated from the segment positions and angles: we expect that entries in this histograms will accumulate around the region where tracks are produced. For every value “ i-th ” of the radius we calculated its corresponding value of z as follows

$$r_{\perp,i} = r_{\perp} - r_i \quad (4.4)$$

$$z_L = z_S - \frac{r_{\perp,i}}{\tan\theta} \quad (4.5)$$

and for each  $(r_{\perp,i}, z_{L,i})$  pair we filled the corresponding bin of the histogram.

### 4.2.3 Results

In Figures 4.5, 4.6 and 4.7, the distribution of straight lines described in the previous paragraph is shown for signal segments. As expected, the most occupied regions of are located at  $(r,z)=(0,0)$  for signal segments, consistent with the fact that the corresponding tracks are originated at the interaction point.

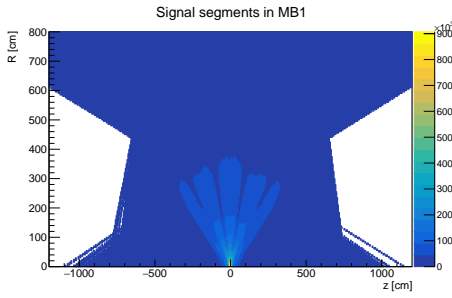


Figure 4.5:  $R - z$  plot of line densities for signal segments in MB1

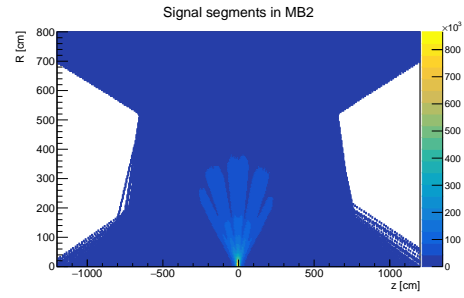


Figure 4.6:  $R - z$  plot of line densities for signal segments in MB2

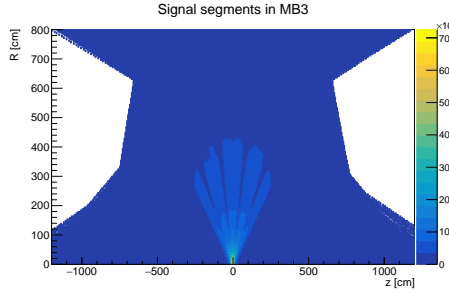


Figure 4.7:  $R - z$  plot of line densities for signal segments in MB3

In Figures 4.8, 4.9, 4.10 we can see the straight line trajectory of background segments. In all three histograms the CMS geometry is clearly visible. For instance, at

the radius value which corresponds to the station position, we can see four low density regions that correspond to the gaps between consecutive wheels where no segment can be reconstructed (see Figure 4.11).

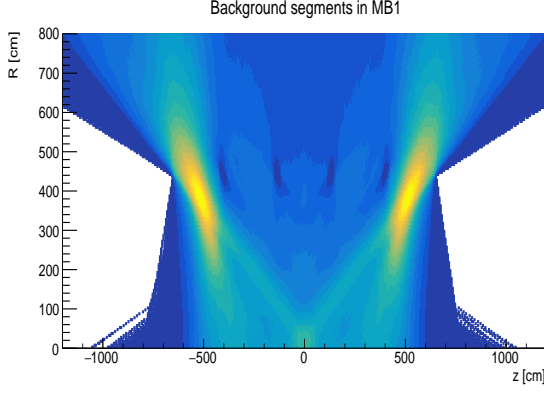


Figure 4.8: Background segments in MB1

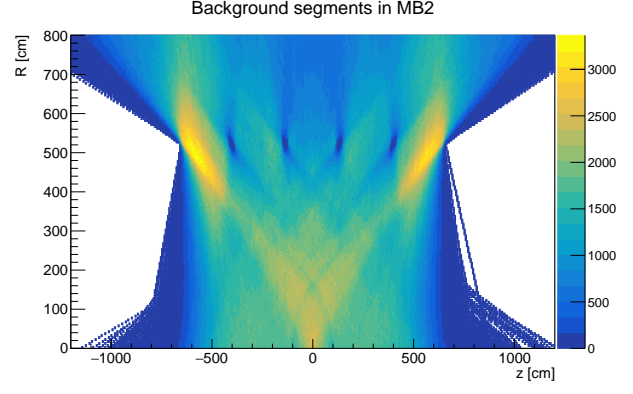


Figure 4.9: Background segments in MB2

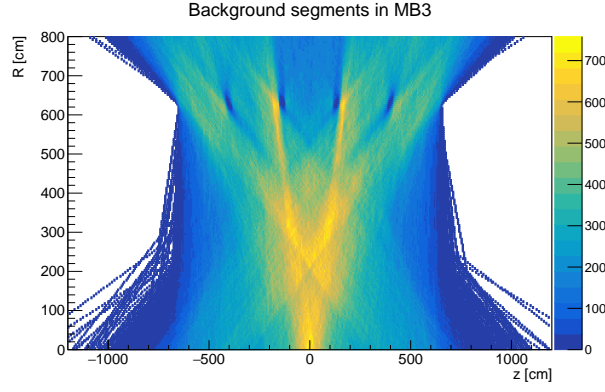


Figure 4.10: Background segments in MB3

In Figure 4.8, where MB1 stations are shown, we can see two outstanding accumulations at about -500 cm and 500 cm on the  $z$  axis and between 400 cm and 300 cm on the  $R$  axis which are supposed to be the origins of background segments. Even if we are considering background segments, some of them are found to point to the interaction point.

In Figure 4.9 the distribution is different. Actually in MB2 stations the accumulations are at larger radius and there are more background segments that point to the origin. Finally in Figure 4.10 we can see that MB3 shows more tracks coming from the interaction region and none at  $|z| \approx 500$  cm. It should be noticed that the maximum of the

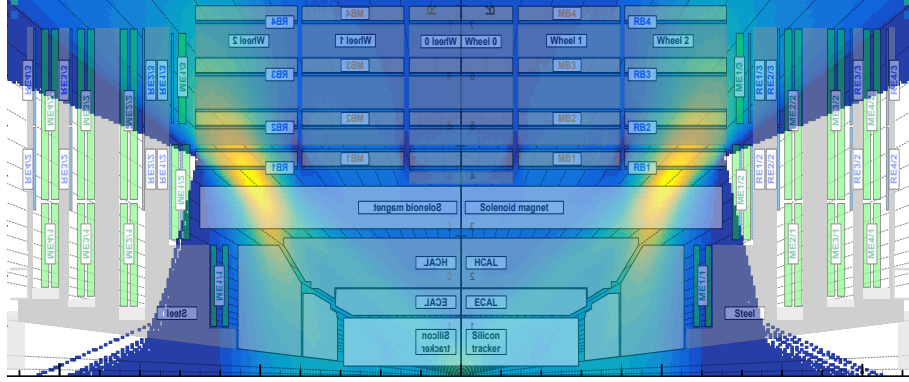


Figure 4.11: Superposition of the MB1 histogram with CMS  $z - R$  section

color scale in the three plots is different from each other. Indeed in MB1 the maximum density value is 30 000, while in MB2 is 3000, and finally in MB3 is 700.

MB1 stations have a very high background which comes from the calorimeter cracks: particles passing through the cracks interact in the solenoid or in the iron yoke, forming the accumulation visible in Figure 4.8. In MB2 stations, we see particles which passed through the cracks but didn't interact before the second iron layer of the yoke between MB1 and MB2. In fact, their density is lower.

Finally, the acceptance of MB3 stations does not cover the cracks and so the two accumulations are no more visible. Another source of background seems to be in the calorimeter, around  $z=0$ : it is well visible in the MB3 (Figure 4.10), less in the MB2 (Figure 4.9) and not at all in the MB1 (Figure 4.8), due to the different color scale.

Finally in all three stations there is a component which comes from the interaction point. These could be segments belonging to muons which were not reconstructed properly or to prompt muons from a different bunch crossing. To verify the hypothesis, we reproduced the graphics dividing in-time from out-of-time segments. Each reconstructed segment has a value of time, derived from the hit fit, referred to the collision time: a perfectly timed segment will have  $t_S \approx 0$ . In order to define in-time segments, we apply a cut on this value,  $|t_S| \leq 13$  ns, while all segments not passing this cut are classified as out-of-time.

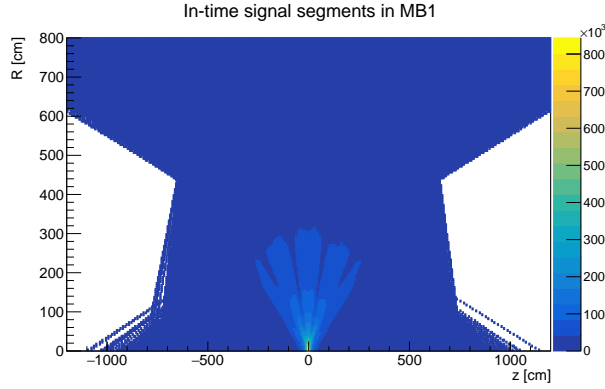


Figure 4.12: MB1 in-time signal

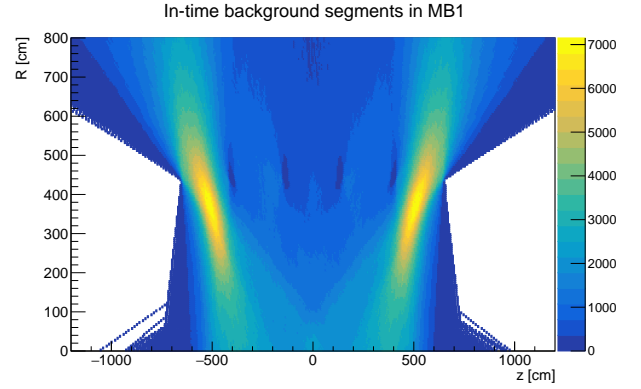


Figure 4.13: MB1 in-time background

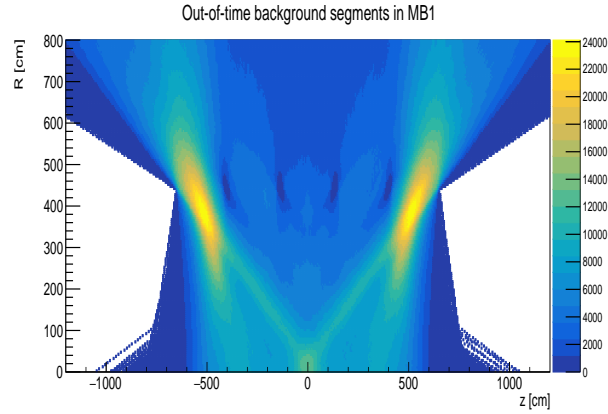


Figure 4.14: MB1 out-of-time background

In MB1 the ratio of entries of in-time background segments (Figure 4.13) and out-of-time background segments (Figure 4.14) is three. Histograms are slightly different from each other. In the out-of-time histograms there are more segments that point to the interaction point, which is consistent with the hypothesis that some of the segments classified as background correspond to prompt muons that could not be reconstructed because they were produced in out-of-time collisions.

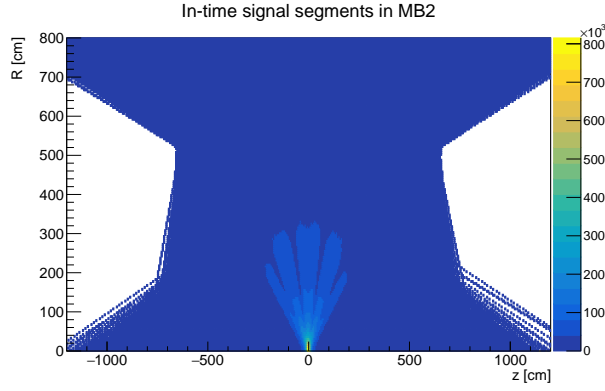


Figure 4.15: MB2 in-time signal

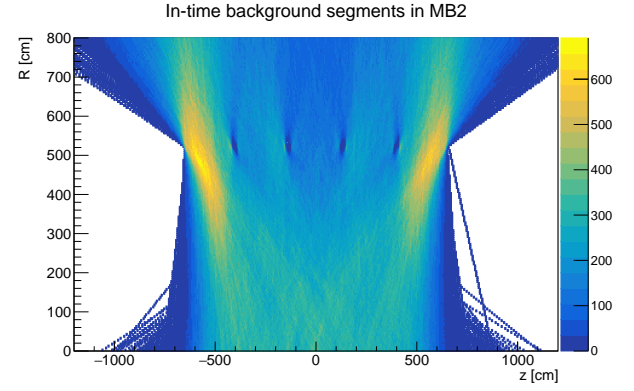


Figure 4.16: MB2 in-time background

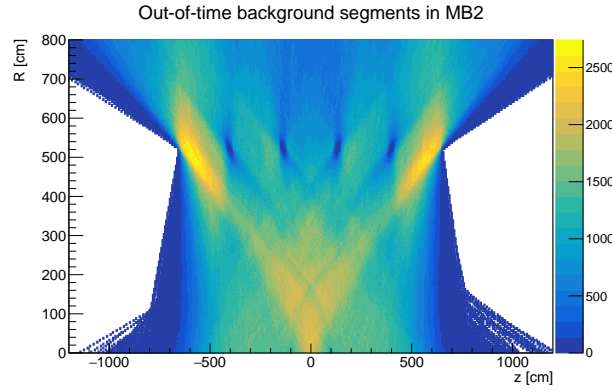


Figure 4.17: MB2 out-of-time background

In MB2 stations the rate of entries of background in-time segments (Figure 4.16) and the entries of out-of-time segments (Figure 4.17) is about 0.27. Again in Figure 4.16 (in-time) we cannot see clear “paths” which point to the IP while, in Figure 4.17 (out-of-time) there is an accumulations near the interaction point.

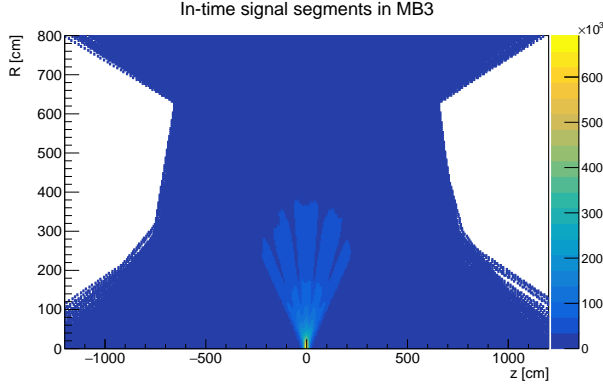


Figure 4.18: MB3 in-time signal

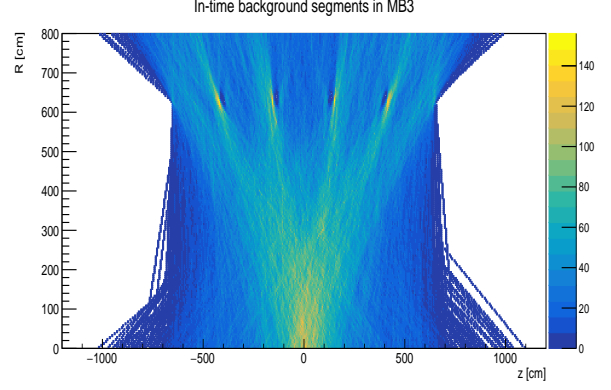


Figure 4.19: MB3 in-time background

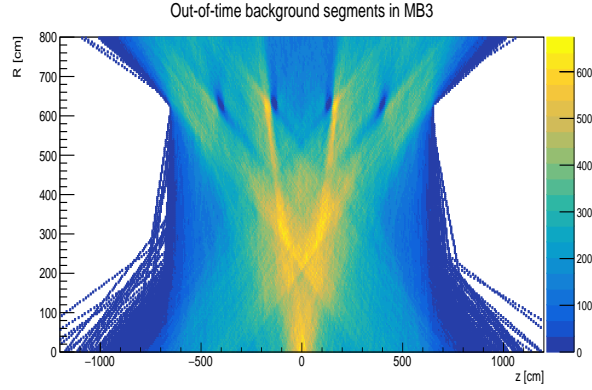


Figure 4.20: MB3 out-of-time background

Finally, in MB3, we find that the rate of entries in the in-time background histogram (Figure 4.19) and in the out-of-time background histogram (Figure 4.20) is about 0.23. In figure 4.19 there is a light accumulation in the IP zone and some points at high density near the gaps between wheels suggesting that signal segments near the gaps failed to be associated to the reconstructed muon whose extrapolation likely passed in the gaps themselves. In Figure 4.20 similar patterns are visible, superimposed to a component originated in the calorimeter.

We can see that the rate of in-time background segments and out-of-time background segments decreases from MB1 to MB3.

Summarizing, we found that:

- some of the segments classified as background seems to be produced by prompt muons from out of time collisions, which are not reconstructed for this reason;
- the contribution of out of time dominates in the outer stations, where the back-

ground rate is overall small; instead, it amounts to only 1/4 of reconstructed background segments in MB1, where the background rate is larger;

- In MB3, also most of the in-time background seems to be due to segments related to prompt muons which were not reconstructed because of acceptance (escaping through the gaps between the wheels).

#### 4.2.4 Background in MB4 stations

The MB4 stations must be studied in a different way. This is because of two reasons. First, because of the lack of the  $\theta$  Superlayer, the MB4 stations don't reconstruct segments in the  $z$  view.

Second, unlike the inner stations, in the MB4 stations we don't expect background from the inside of the detector, but background produced by so called neutron gas and coming from above the detector.

Neutrons are originally produced by secondary interactions in the detector material and especially in the calorimeters. They diffuse outside like a gas, reach thermal energy and fill the empty space between the detector and the cavern ceiling. From there, they will randomly hit back the detector and, through nuclear capture, produce very soft electrons which in turn ionize the DT gas and give signals.

It is supposed that this mechanism is confined in one cell volume, but actually low quality segments are also reconstructed (Figure 4.21). The mechanism is under investigation. Two hypotheses were considered: segments could originate from casual alignments of background hits or they could be produced by electronics crosstalk.

Considering the first hypothesis we calculated the probability of the casual alignment of three hits.

We started from calculating the surface of the cell which is  $S=1023 \text{ cm}^2$ , hence the rate could be seen as  $S \cdot R$ , where  $R=7\text{Hz}/\text{cm}^2$ . Then, the average number of hits per event is  $\text{rate} \cdot 400\text{ns}$ , where 400ns is the drift time. Finally, using the Poisson distribution

$$P_{\lambda}(n) = \frac{\lambda^n}{n!} \exp\{-\lambda\}, \quad (4.6)$$

we calculated the probability of a casual alignment of three hits and we found that this latter is  $P < 3 \cdot 10^{-8}$ .

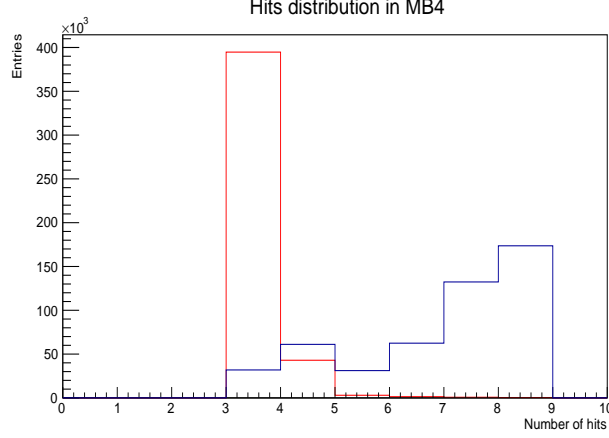


**Figure 4.21:** Number of hits associated to reconstructed background (red) and signal (blue) segments in MB4

We repeated the study performed with MB1, MB2, MB3 for the MB4, but this time on the  $R - \varphi$  plane. Only prompt muons with a high transverse momentum, and hence almost no bending arrive in MB4 stations as we can see from Figure 4.23. Background segments instead concentrates in the top sector and their origin seems to be immediately outside the detector (Figures 4.22, 4.24). From Figure 4.24 it can be seen that the level of background in the top sector is lower than that in the adjacent sectors because of the shield of lead and polyethylene, which is under construction for the other sectors.

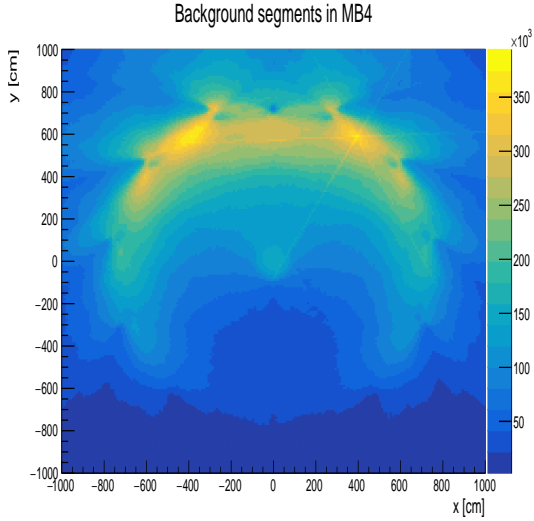


**Figure 4.22:** Transverse view of background segments in MB4

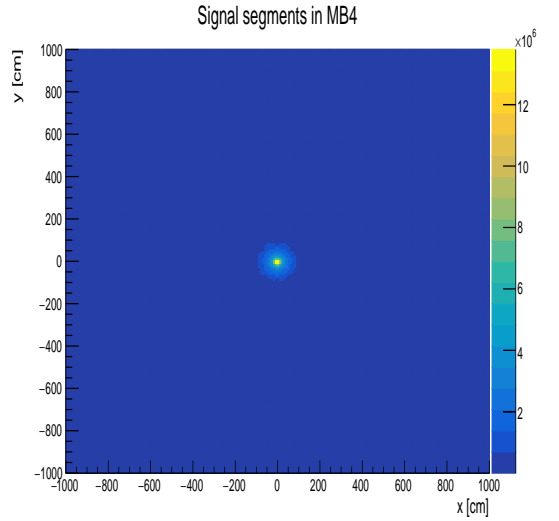


**Figure 4.23:** Transverse view of signal segments in MB4



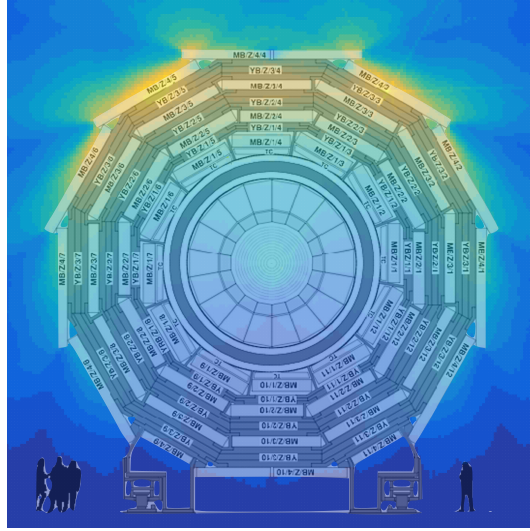


Figure 4.24: Superposition of the MB4 histogram and the CMS transverse cross section

In the previous plots (Figures 4.22,4.23) we focused on the global reference system. Now, considering the chamber local reference system in the  $R - \varphi$  view, we obtain the distribution of local direction of signal and background segments.

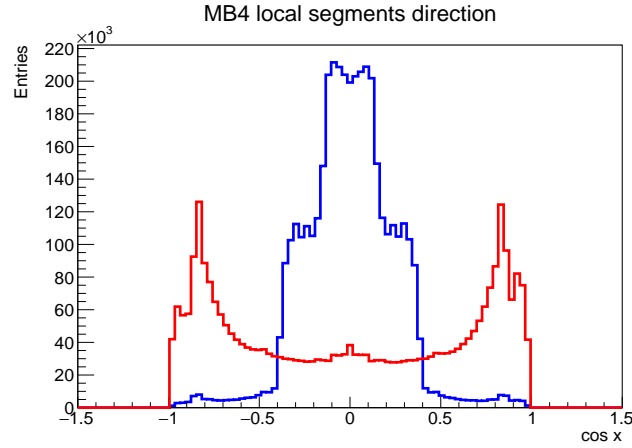


Figure 4.25: MB4 background (red) and signal (blue) local segments direction

In figure 4.25 signal (blue) and background (red) are clearly different. Considering signal segments, we can see that they peak at 0 as we expected. Actually only prompt muons with enough transverse momentum arrive at the MB4 stations, with little bending and hence almost perpendicular to the chamber. This can be seen even in Figure 4.23, where high transverse momentum prompt muons in MB4, extrapolated as straight lines, head to the interaction point. Instead, background distribution has two peaks at about

-0.8 and 0.8 from which we can assume that background segments hit the station with high inclination. This means that, as we can see from figure 4.25 background segments do not come from the interaction point, but could come from the neutron gas outside the detector.

# Conclusions

High levels of background can cause early ageing of the detector and could affect the muon trigger performance and pattern recognition of muon tracks. This thesis focuses on the study of background segments in the drift tube chambers of the CMS detector. In fact segments are used to seed the muon reconstruction, therefore they may also affect the physics analysis.

Our main goal was to assess the origin of background segments in the innermost and outermost stations. We adopted a definition of background, where we consider as background whatever signal is not associated to a reconstructed crossing muon. In order to visualize the origin of background segments, we built two-dimensional histograms where we superimposed the straight lines derived from segment extrapolation: actually entries in this histograms will accumulate around the region where tracks are produced. For each station we obtained two histograms: for signal and background. Signal histograms were more or less identical to each other, with only one peak at the interaction point as expected. Conversely, background histograms were different from each other. In the two inner stations we have two high density points at approximately  $(z,R)=(-500,400)$  cm and  $(z,R)=(500,400)$  cm, which correspond to the regions just outside the cracks, between the barrel and endcaps calorimeters. In addition some components are visible that point to the interaction point. These are dominant in the third station where acceptance doesn't cover the calorimeter gaps. They appear to be produced by signal segments that failed to be associated to reconstructed muons (these accumulate near the gaps between wheels), or signal segments associated to out-of-time muons. To investigate these features we refined the analysis dividing in-time from out-of-time segments. We also studied background segments in the fourth station where the  $z$  information is not available. We repeated the study performed on the inner stations but this time on the  $R - \varphi$  plane. Again signal segments point to the interaction point and form a clear peak in  $(x=0,y=0)$ . Background segments concentrate in the topsectors and their origin seems to be immediately outside the detector. This is consistent with the hypothesis that background in the top external chambers is produced by a gas of thermal neutrons setting up in the experimental cavern.

# Bibliography

- [1] CMS collaboration, *Performance of the CMS muon detector and muon reconstruction with proton-proton collisions at  $\sqrt{s} = 13$  Tev* 2018
- [2] CMS collaboration, *The performance of the CMS muon detector in proton-proton collisions at  $\sqrt{s} = 7$  Tev at the LHC* 2014
- [3] Masetti G, Cavallo F, *Collision induced background in the DT chambers* 2013
- [4] Guiducci L, *(Private communication)*
- [5] Cavallo F, *(Private communication)*
- [6] Bonelli G, *Study of the background induced by LHC colliding beams in the Muon Barrel Detector of CMS* 2017
- [7] <https://cms.cern>
- [8] <http://www.root.cern.ch>